Key Points:
- PMC albedo and T zonal variations are anticorrelated in season start and end
- But in the core of the season albedo and T correlation is relatively poor
- Cloud albedo and water vapor are poorly correlated owing to vapor depletion

Northern PMC brightness zonal variability and its correlation with temperature and water vapor

P. P. Rong[1], J. M. Russell III[1], C. E. Randall[2], S. M. Bailey[3], and A. Lambert[4]

[1]Center for Atmospheric Sciences, Hampton University, Hampton, Virginia, USA, [2]Laboratory for Atmospheric and Space Physics, University of Colorado, Boulder, Colorado, USA, [3]Bradley Department of Electrical and Computer Engineering, Virginia Polytechnic Institute and State University, Blacksburg, Virginia, USA, [4]Jet Propulsion Laboratory, California Institute of Technology, Pasadena, California, USA

Abstract Polar mesospheric clouds (PMCs) measured by the Cloud Imaging and Particle Size instrument on the AIM satellite show strong zonal asymmetries, with prominent planetary-scale variations. The correlations between zonal variations of cloud brightness and temperature or water vapor (H_2O) are determined in different stages of the PMC season. Aura Microwave Limb Sounder measured temperature and water vapor are used in the analysis. A zero-dimensional (0-D) PMC model was used to interpret the observation. Analyses of all days of the five northern seasons from 2007 to 2011 indicate that temperature and albedo daily zonal variations are anticorrelated in the season start and end, whereas in the core of the season the correlation is relatively poor. The albedo and H_2O correlation in the zonal direction is poor throughout the season. Zero-dimensional model physics indicates that when clouds are weaker, or the environment is warmer and drier, temperature plays an increasingly important role in determining the cloud ice mass variation, which explains the stronger correlation of temperature and albedo at the start and end of the season. Water vapor takes a strong role in determining the ice mass variation in the core of the season when the clouds are stronger and the environment is colder and wetter. However, on a daily basis the H_2O depletion associated with the ice production will lead to significant shift of the ice maxima and "post-ice" H_2O maxima in the zonal direction, which leads to the poor correlation between the observed H_2O and albedo.

1. Introduction

The Cloud Imaging and Particle Size instrument (CIPS) [*McClintock et al.*, 2009; *Rusch et al.*, 2009] on the AIM satellite (AIM) [*Russell et al.*, 2009] has been routinely taking global polar mesospheric cloud (PMC, or noctilucent cloud) images since May 2007, and from these images, cloud albedo, column ice, and ice particle radius are retrieved. The purpose of this study is to determine the correlation between daily planetary-scale cloud brightness variations and the environment temperature and water vapor in different stages of the cloud season. The CIPS daily cloud albedo and the corresponding temperature and water vapor measured by the Microwave Limb Sounder (MLS) on the Aura satellite [*Waters et al.*, 2006] are used. The intraseasonal variation of the correlation is further interpreted via applying a 0-D PMC model [*Hervig et al.*, 2009]. The 0-D model physics is used to assess the relative roles of temperature and water vapor in determining the cloud ice mass density variation.

The spatial variation of PMCs in the horizontal direction and its correlation with the environment temperature (or water vapor) has been less studied prior to AIM because of various limitations that are related to data availability. Contemporaneous observations are required between the measured PMCs and temperature (or water vapor) to investigate their correlated relationship. Thermosphere Ionosphere Mesosphere Energetics and Dynamics (TIMED) Sounding of the Atmosphere using Broadband Radiometry (SABER) instrument [*Russell et al.*, 1999] (2002 to present) on the Thermosphere Ionosphere Mesosphere Energetics and Dynamics satellite and Aura MLS (2005 to present) are two primary data sets that provide the global-wise middle to upper atmosphere temperature and water vapor measurements, although the SABER water vapor product is still in the testing stage and has not yet been released. Considering the mission span of these data sets, potentially suitable PMC data sets include those taken by the Student Nitric Oxide Explorer (SNOE) (1997–2003) [*Bailey et al.*, 1996; *Solomon et al.*, 1996], Optical Spectrograph and Infrared Imager System (OSIRIS) (2002 to present) [*Llewellyn et al.*, 2004], and AIM CIPS (2007 to present). For example, *Merkel et al.* [2008] used SNOE and SABER to investigate the planetary modes in both PMCs and temperature. Nevertheless, SNOE ceased operation before or around the time of Aura satellite launch, and

therefore it cannot be used to confirm the results of this paper. The OSIRIS data set has global coverage, can detect weak clouds, and has, so far, over a decade of measurements, but its data consistency is more or less affected by the intermittent switch off of the mesospheric measuring mode. As a result, it requires a more comprehensive technique to sample the OSIRIS PMC data set to study the PMC spatial variability [e.g., *Hultgren et al.*, 2012]. Solar Backscatter Ultra-Violet series (SBUV, 1978 to present) [*DeLand et al.*, 2003] offers by far the longest data set for PMC climatology, but as it measures a subset of the clouds, is less appropriate than CIPS for the present task.

Most satellite data sets consist of 14–15 orbits per day therefore can achieve a ~20° longitudinal resolution. The CIPS data set, which consists of orbital strips, achieves much higher horizontal resolution (i.e., 25 km^2), full polar daily coverage throughout any given season within the AIM mission period, and can resolve both weak and strong clouds except for some of the weakest clouds in the lower latitude (i.e., < 60°N/S). CIPS data set therefore greatly benefits the studies that address the small-scale cloud structures, but even if we focus on the planetary-scale cloud variations, the high resolution can still be advantageous because the large-scale components will be more accurately extracted from a wider spectrum of scales. The availability of CIPS and MLS data together on the same time period since 2007 made it possible to study the relationship between clouds and environmental temperature and water vapor on time scales both short and long. Furthermore, the fact that the daily polar coverage is achieved throughout the season and for all years available makes the results of the analysis more reliable in a statistical sense.

The spatial variability of PMCs can be highly complex because different processes may control the cloud variations. Microphysics in response to the environment temperature and water vapor is the key controlling process that is characterized by the cloud genesis and sublimation processes with time scales of a few hours to a day. In addition, dynamical effects such as advection, planetary and gravity waves, and tides can also control the PMC variation through changing the environment temperature and water vapor or through directly interfering with the cloud genesis and sublimation processes. For example, *Chandran et al.* [2012] found that long or short wavelength gravity waves either temporarily enhance or weaken the cloud brightness through interfering with the cloud sublimation or genesis. *Baumgarten et al.* [2012] found that zonal winds can blow the clouds downstream several hundred kilometers if no wave structures are involved. PMCs vary over a hierarchy of time scales and can appear highly unpredictable. For example, the overlapped CIPS images between consecutive orbits, which occur about 90 min apart, indicate that a cloud structure can remain roughly unchanged over several orbits but also can change from orbit to orbit, depending on the dynamical condition. Such unpredictability may lead to poor spatial correlations between the daily PMCs and temperature (or water vapor) and makes it challenging to interpret the results.

Smaller scale and relatively localized PMC features vary more rapidly, and most of the unpredictability in PMCs comes from such rapid variations. But if we ignore the small-scale variations and focus on planetary-scale variability, the cloud structures will likely be longer lived. The wave-1 component, for example, may last longer than a day. If the large-scale cloud features do live up to a day, any concerns about poor temporal and spatial coincidences between measurements are greatly lessened. This then will facilitate this current study because CIPS and MLS instruments are known to show poor coincidences; both Aura and AIM satellites are in Sun-synchronous polar orbits with equator crossing times at 12:00 am and 1:45 pm (ascending/north going), respectively; for a given UT time, in the 65° to 85°N latitude range; CIPS and MLS data points show poor longitudinal coincidences throughout the northern summer.

Studies by *Merkel et al.* [2008, 2009] indicated that SNOE and CIPS PMC brightness and frequency have shown westward traveling features, reflecting a 5 day planetary wave-1 component. The same component was found in the SABER temperature with a nearly 180 phase shift from the cloud phase. It was concluded that temperature is an important forcing mechanism for planetary-scale variations in PMCs. *Nielsen et al.* [2010] found that the 5 day wave activity is prominent in August and can serve to extend the PMC season. Planetary-scale disturbances are likely the main contributors to the global-scale PMC variations shown in CIPS global maps. In these previous studies the individual planetary-scale components in both PMCs and temperature are identified and their connections are investigated. Given these existing large-scale varying modes, in this study we will examine the relative roles of temperature and water vapor in determining the ice mass variation and how these roles change over the cloud season. In section 2 we describe the data sets and the 0-D model [*Hervig et al.*, 2009] used for data interpretation. Results of a correlation analysis with the five years of observations are discussed in section 3. A "pre-ice" water vapor
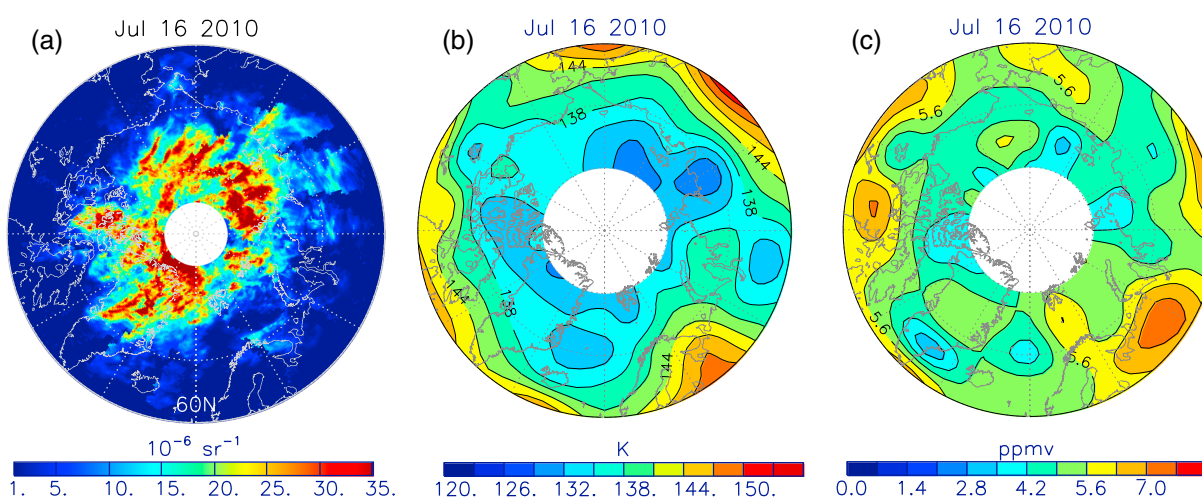
Figure 1. (a) Polar maps of CIPS daisy, (b) MLS temperature, and (c) MLS H_2O north of 60°N on the 16 July 2010. All data points of CIPS daily daisy are overplotted, while MLS temperature and H_2O at pressure level of 0.00464 hPa are interpolated onto 20°longitude × 5°latitude grids.

(H_2O) condition is constructed and discussed in section 4. In section 5 we discussed the nominal 0-D model results and 0-D physics in terms of how temperature and water vapor control the ice mass density variation. In section 6 an adjusted 0-D model is used to interpret the correlations between cloud mass density and water vapor at the season start and end, and furthermore, temperature and water vapor correlation is discussed. Conclusions are given in section 7.

2. Data Sets and 0-D Model

2.1. Data Sets

The fundamental basis of the CIPS data retrievals is described by *Bailey et al*. [2009], and the v4.20 retrieval algorithm, which is the version used here, is described in detail by *Lumpe et al*. [2013]. CIPS PMC detections and albedo have been evaluated by *Benze et al*. [2009, 2011]. Each day CIPS observes the summer polar region from ~40° to 86° latitude with 25 km^2 spatial resolution; most clouds are detected poleward of ~55°. For this paper we use the CIPS level 3 albedo data product. This data product, which consists of a daily polar map of the PMC albedo, is commonly referred to as the daily "daisy." The daily daisy is generated by combining the measured albedo values from all of the individual orbit strips (level 2 data) on a given day into a single image covering the summer polar region. When pixels from different orbits overlap, which occurs poleward of ~75° latitude in each hemisphere, the brightest pixel (not the average) is used. Both the ascending and descending node data are combined in the level 3 data product, so there is no time selection criterion. Only data points for which the scattering phase function was measured at a minimum of four different scattering angles are included in the daisies. As an example, Figure 1a shows the original daily daisy for 16 July 2010, or 25 days from summer solstice (DFS hereinafter).

Aura MLS (MLS hereinafter) version 2.2 temperature and H_2O volume mixing ratios (VMRs) [*Schwartz et al*., 2008; *Lambert et al*., 2007] are used to carry out the correlation study with CIPS albedo and the PMC model simulations. Figures 1b and 1c show interpolated maps of MLS temperature and H_2O on the same day as in Figure 1a, on the 0.00464 hPa pressure level (~84 km). There appears to be a large-scale correspondence between high PMC albedo and low temperatures. While for water vapor the correspondence in the zonal direction is not clear, there appears to be a systematic depletion feature poleward of 70°N. The MLS data are interpolated onto 20° longitude × 5° latitude grids, and such a grid size is universally adopted in this study. The vertical resolutions of MLS temperature and H_2O VMR profiles in the mesosphere are ~10 km and ~15 km, respectively, so choosing the 0.00464 hPa is to approximately match with the PMC centroid altitude or cloud base [*Chu et al*., 2001; *Jensen and Thomas*, 1988]. MLS resolution being ~10 to 15 km would be a concern because PMCs are considered a thin layer that spans the mesopause region (~80–90 km) and is centered at ~83–84 km. Nevertheless, the actual vertical spacing of the MLS data is much finer, which is about 3–4 km, and it appears that vertical structural difference can be resolved pretty well in MLS data (see section 4) unless

the feature to be resolved is extremely narrow (~1–2 km). In this later case the feature will be significantly broadened. For example, the enhancement layer (80 ± 1 km altitude) caused by the ice sublimation [*Summers et al.*, 2001] is broadened into 5–10 km in the MLS H_2O [*Rong et al.*, 2011].

2.2. 0-D Model

A 0-D model [*Hervig et al.*, 2009] is used in this study. The model assumes a thermal equilibrium between the bulk ice and the vapor phase of H_2O, and ignores nucleation, sedimentation, horizontal transport, the time dependence of ice growth and sublimation, and the effect of particle size on saturation vapor pressure (the Kelvin effect). The original 0-D model is given in equation (2) of *Hervig et al.* [2009]; nevertheless, in this study the model is expressed in terms of water vapor pressure (P_{H2O}) and saturation vapor pressure (P_{SAT}), i.e., 100% of P_{H2O} in excess of P_{SAT} is turned into ice. P_{SAT} and P_{H2O} are model input and ice mass density (m_{ice}) is the model output, given by formula

$$m_{ice} = (P_{H2O} - P_{SAT})/T/R \cdot 10^9 \cdot M_{H2O} \tag{1}$$

where T is temperature, R is the gas constant, and M_{H2O} is the water vapor molecular weight. The factor 10^9 indicates that m_{ice} is given by ng/m^3. The term "excess H_2O," defined as $P_{H2O} - P_{SAT}$, will be regularly used in the remainder of this paper. The *Murphy and Koop* [2005] formula is used to calculate P_{SAT}. Ice exists when P_{H2O} is greater than P_{SAT}, or temperature is below the frost point. Furthermore, terms pre-ice H_2O and post-ice H_2O are defined because they are key variables to interpret the 0-D model results in the current study. The pre-ice H_2O simply refers to P_{H2O}, while the post-ice H_2O refers to the residual part of pre-ice H_2O with the water ice being subtracted, defined as

$$P_{H2O} - (P_{H2O} - P_{SAT}) \cdot F = (1.0 - F) \cdot P_{H2O} + P_{SAT} \cdot F \tag{2}$$

where F refers to the fraction of "excess" H_2O that is converted into solid phase. In the original 0-D assumption F is 1.0, in which case the post-ice H_2O will simply be P_{SAT}. When divided by the air pressure, i.e., 0.00464 hPa, pre-ice and post-ice H_2O are also expressed by VMRs. The pre-ice H_2O is the water vapor condition before the ice is formed, while the post-ice H_2O refers to the actual measured water vapor with the ice present. In the following part of the paper we will find that the spatial distributions of the two variables can be drastically different owing to the ice production process.

In this study the 0-D model is used to examine the correlation of m_{ice} and temperature (or water vapor) variations in the zonal direction. The modeled correlation will be compared to the CIPS albedo and temperature (or water vapor) correlation. As is mentioned above, in the 0-D model the processes of nucleation and atmospheric dynamics are ignored; as a result, the ice production does not experience any developing stage, but responds immediately to the in situ temperature and water vapor. Therefore, the 0-D modeled clouds represent PMCs that are in their developed or matured stages. Each coincident measurement of MLS temperature and water vapor is used to calculate the ice mass density (m_{ice}) at 0.00464 hPa. In this study, m_{ice} is used as a proxy to albedo because the largest particles that had major contribution to the albedo are located at the cloud base or "virtual height" where the maximum ice particle radius occurs [*Jensen and Thomas*, 1988]. Also, PMCs simulated by the Community Aerosol and Radiation Model for Atmospheres (CARMA) have shown approximately aligned peak altitudes for ice particle mean radius, ice mass density, and backscatter ratio [*Rapp et al.*, 2002]. However, the correspondence between the large ice particle size and brighter clouds is not always the case. For example, recent findings using the CIPS data confirmed the existence of large ice particles with low albedo and Ice Water Content (D. W. Rusch, AIM team meeting, 2013). These conditions generally occur at times of low cloud albedo and Ice Water Content and likely at the lower altitude rather than at the cloud centroid altitude. Some of them are apparently associated with the gravity wave signatures. Therefore, these cases will not affect the general basis of this paper. The 0-D model has been proven to be highly effective in reproducing PMC variations in several cases. For example, *Hervig et al.* [2009] has shown that intraseasonal variation of ice mass density agrees very well with the AIM Solar Occultation for Ice Experiment (SOFIE) observations. *Rong et al.* [2012] indicated that on intraseasonal scales, CIPS PMC frequency variations show strong agreement with SOFIE observations. The 0-D model works best when PMCs are in their developed stages and are not subjected to rapid changes that will interfere with the natural course of cloud genesis and sublimation in response to the given environment temperature and water vapor. As mentioned above, such rapid changes can be induced by both gravity waves and advection [*Chandran et al.*, 2012; *Baumgarten et al.*, 2012]. Adopting the 0-D model for a study of PMC spatial variations on a daily
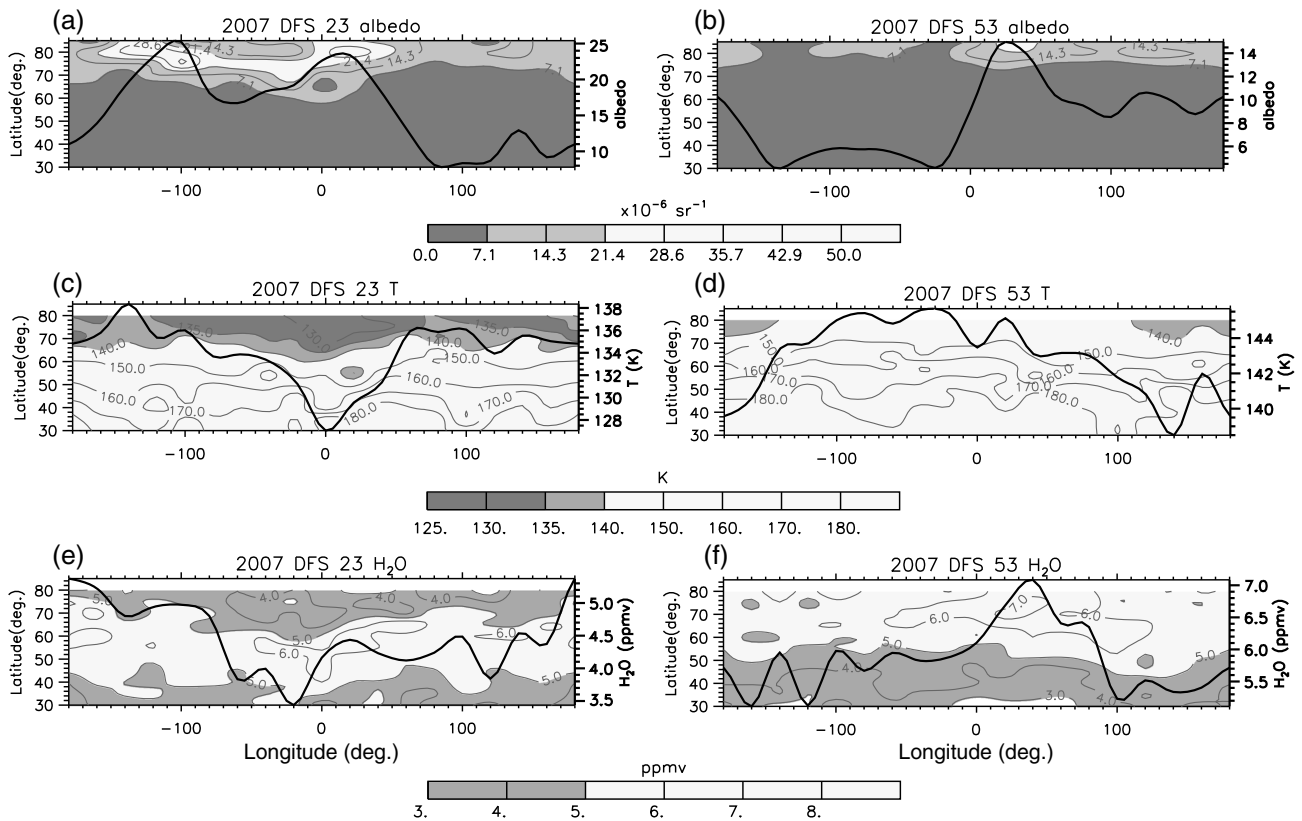
Figure 2. (a, b) Longitude versus latitude gridded fields of CIPS albedo, (c, d) MLS temperature, and (e, f) H_2O. The negative longitudes represent the west hemisphere and vice versa. The corresponding data points are interpolated onto the 20°longitude × 5°latitude grids, and the average of the data points that fall into each grid is taken as the grid value. The left and right panels represent the time frames in the core of the season and at the end of the season, respectively. The thick black curves are zonal series averaged north of 70°N. The magnitude of the zonal series is indicated on the right axis.

time scale poses greater challenges because advection and gravity waves may play roles. These rapid processes along with the poor coincidences between the AIM CIPS and Aura MLS orbital tracks will result in the modeled and observed PMCs being inherently different. However, we have argued above that global and large-scale cloud features are expected to be longer lived, in which case the 0-D model will remain effective.

3. Observations

To illustrate how temperature and water vapor control the global cloud brightness variation in different stages of the season, we first show two individual days, 23 DFS (14 July) and 53 DFS (13 August) 2007, that are representative to the core and end of the season. For each given day, we compare the global maps of CIPS albedo, MLS temperature, and water vapor, shown in Figure 2. Since the CIPS and MLS data have such different spatial resolutions, both data sets have been binned to a uniform grid of 20° longitude × 5° latitude, with each grid value taken as the average of all data that fall within ±10° in longitude and ±2.5° in latitude of the grid point. On average, each grid point thus represents about 5–9 measurements from MLS, and about 6000–12,000 data points (with albedo > 0) from CIPS. For CIPS the exact number of data points decrease significantly when latitude is greater than 80°N, but this should not affect the mean values within each grid since the sample number is large enough to be representative. Figure 2 shows both the gridded data (contours) as well as a polar average (thick black curve). The polar average, referred to as a zonal series in the remainder of this paper, is formed by averaging data north of 70°N within each longitude bin. The zonal series analysis is applied to the region north of 70°N because the CIPS orbits overlap in this latitude region, so there are no data gaps. In addition, the CIPS cloud detections are less robust at lower latitudes. This is related to the fact that the lower latitudes correspond to either the highest or lowest solar zenith angles (SZAs) sampled by CIPS. As described by *Lumpe et al.* [2013], the CIPS cloud detection rate decreases with decreasing SZA, where
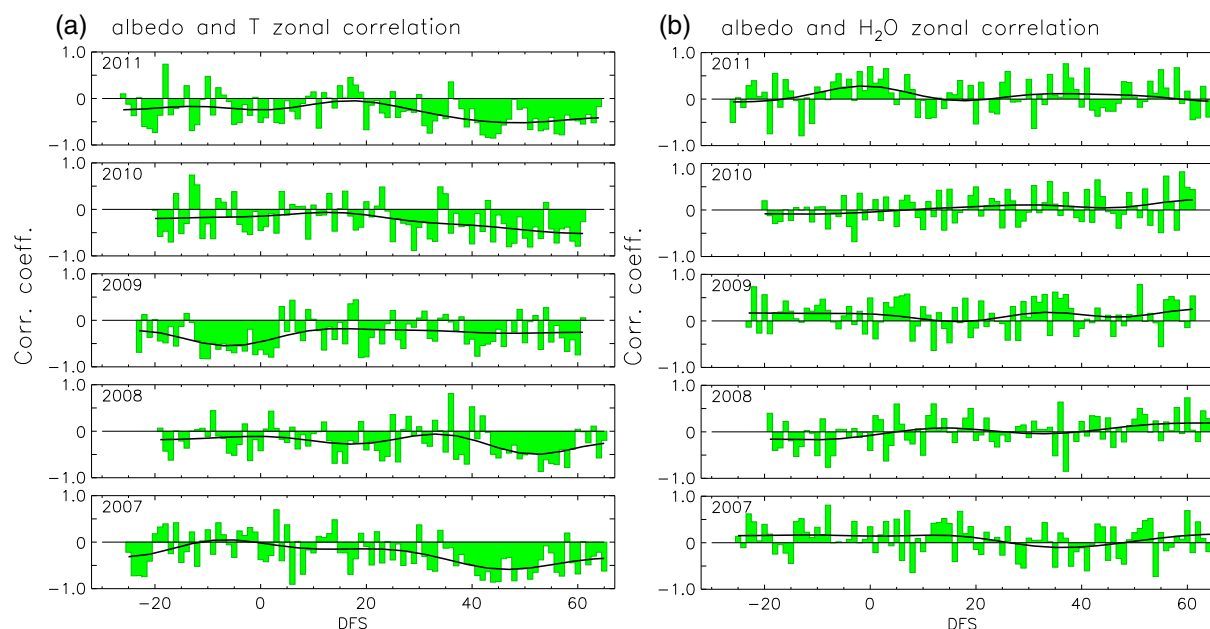
Figure 3. Intraseasonal variations of the correlation coefficients of the zonal series for the five northern PMC seasons from 2007 to 2011. The zonal series is generated using the averaged values north of 70°N. This applies to all the correlation coefficients shown in this paper. (a) The albedo versus temperature correlation coefficients. (b) The albedo versus water vapor correlation coefficients. The thick black curves are the 16 day smooth of the daily data.

the background Rayleigh scattering is higher. On the other hand, false detections increase at the highest SZAs where the Rayleigh scattering changes rapidly with SZA. Largest errors occur for SZA $<42°$ or $>95°$, which correspond to latitudes between 50°N/S and 65°N/S. Although we focus on the high-polar latitude region ($> 70°N$) where PMCs are the brightest and most abundant, we show maps north of 30°N to be able to clearly observe the temperature and water vapor variation from no-cloud to cloud regions in the latitudinal direction.

In both the left and right panels of Figure 2 large-scale temperature and albedo variations are roughly anticorrelated in the zonal direction, with brighter clouds corresponding to lower temperatures. However, water vapor and albedo correlations are different in the two stages of the season; on 23 DFS, the brighter clouds correspond to the drier section and vice versa; it is the opposite on 53 DFS. This suggests that water vapor depletion occurs when a larger percentage of water vapor is turned into ice, which occurs in the middle of the season. Driven by the same mechanism, in the latitudinal direction on 23 DFS there is a distinct depletion zone in the polar region, while at the end of the season there is no such zone and water vapor monotonically increases toward the higher latitude. Figure 2 is shown to illustrate some key mechanisms of the relationship between cloud brightness and temperature (or water vapor), whereas the main goal of this paper is to draw general conclusions that characterize all individual days. What is shown in Figure 2 does not represent the entire ensemble of cases because the relative positioning between the wet and cold sections can be highly variable depending on the individual days, and the overlap of the wet and cold sections will necessarily result in the most efficient ice production.

Figure 3a shows the correlation coefficients of the albedo and temperature zonal series throughout the cloud season. The correlation coefficients of albedo and water vapor are shown in Figure 3b. Five northern seasons from 2007 to 2011 are included. The seasonal variations of the correlations are generally consistent between the years examined; for example, throughout the season, albedo and temperature remain anticorrelated, while albedo and water vapor show overall extremely poor but slightly positive correlation. A close look at the data indicates that the anticorrelation of albedo and temperature is often stronger toward the start or end of the season, whereas in the core of the season, it is relatively poor. However, there are exceptions, for example, in 2008, a 2 week period stands out in the core of the season during which the anticorrelation remains fairly strong. The core period versus season end/start is better characterized by the 16 day smoothed curves. The season start and end in this context refer to periods with a substantial length, together taking up

two thirds of the cloud season. Previous work has defined the basic roles of temperature and water vapor in different stages of the PMC season. *Rong et al*. [2012] argued that temperature plays a strong role in controlling the onset and termination of the cloud season, which is generally consistent with what is shown here, but this argument is insufficient to interpret the intraseasonal variation. Compared to what is shown in *Rong et al*. [2012], the core period in Figure 3a either appears short or there are simply no clearly defined start and end periods. This is because in *Rong et al*. [2012] the cloud frequency rather than cloud brightness is used. Cloud frequency can be saturated to 100% regardless of how strong the clouds are, resulting in more rapid transition between the season start, core, and end. We also note in Figure 3a that correlations toward the start and end show asymmetric development, with the period toward the end more prolonged and showing more robust anticorrelation. This is related to the fact that the coldest day in summer, which in many cases occurs around the summer solstice, is closer to the start than to the end of the cloud season. The albedo and temperature correlation on the coldest day should minimize because the dependence of ice mass density on temperature reduces to a very low level when temperature is far below the frost point. *Rong et al*. [2012] also argued that water vapor plays a dominant role in controlling the core period ice mass density variation. PMCs in the core period are generally stronger, and the cloud particle sizes have grown large enough to descend from the formation region around the mesopause to the growth region at ~83 km where water vapor is more abundant [*Megner*, 2009]. However, there is no indication from Figure 3b that water vapor has any consistent correlation with albedo, which appears to contradict a strong control of water vapor on the cloud brightness variation. This contradiction characterizes a key difference between the daily scale studied here and the intraseasonal-scale variations described in *Rong et al*. [2012]. In the following sections we will use the 0-D model results to interpret the seasonal development of the correlation coefficients between albedo and temperature (or water vapor).

4. Pre-ice Conditions for 0-D Model Simulations

To perform the 0-D simulations we set up the pre-ice H_2O (see definition in section 2.2) and temperature conditions. It is more satisfying to construct a pre-ice H_2O since using the water vapor profiles with the depletion feature as the model input does not adequately reflect the cloud physics. The water vapor depletion causes significant difference in the H_2O spatial distribution before and after the ice production, with a majority of measured water vapor profiles exhibiting depletion features that led to the systematic polar depletion (Figure 2e). The temperature variation, on the other hand, overall has more robust features and is less affected by the existence of ice particles. To set up an appropriate pre-ice H_2O we either restore it through combining the observed ice and water vapor or set up a water vapor condition that mimics the pre-ice state. Combining the CIPS column ice and MLS column water vapor is a viable approach, but it will induce large uncertainties from each data set; the poor vertical resolution of the MLS H_2O VMR profile will result in large uncertainty in the corresponding MLS column water vapor. In addition, the CIPS column ice has not yet been validated. Since accounting for these uncertainties goes beyond the scope of this study, we choose a water vapor condition that can be used as a pre-ice proxy. This latter approach is less straightforward, but is just as valid for implementing the 0-D calculations. In each 20°lon × 5°lat grid box the H_2O VMR that leads to the maximum m_{ice} is chosen. To obtain such a pre-ice H_2O we first run 0-D model for all pairs of MLS temperature and H_2O in a given grid box and then select the H_2O corresponding to the maximum m_{ice}. In most cases the chosen value is the maximum H_2O VMR within that grid box unless the corresponding temperature is either too close or above the frost point. It was mentioned above that the pair of temperature and water vapor measurements must come from the same MLS event, and when temperature approaches the frost point there is either no cloud or a weak cloud, regardless of the given H_2O abundance. At the low latitudes where no 0-D ice exists, we simply choose the maximum H_2O within a given grid to maintain data consistency. Figure 4 shows the latitude versus time intraseasonal variation of water vapor in 2010. Year 2010 is chosen as an example and all other years have shown similar characteristics. Figures 4a and 4b show the zonal means of all events that fall into each latitude bin and the zonal means of the grid-based pre-ice H_2O VMRs just chosen, respectively. In Figure 4a there is a clearly defined polar depletion zone that gradually retracts toward high latitudes as the season progresses, while in Figure 4b no such zone exists and water vapor increases with time and latitude. Such a large difference between the pre-ice and post-ice H_2O indicates that the depletion caused by water ice production can drastically change the water vapor horizontal distribution. The asymmetry of the depletion zone between the start and end reflects the fact that water vapor builds up persistently throughout the cloud
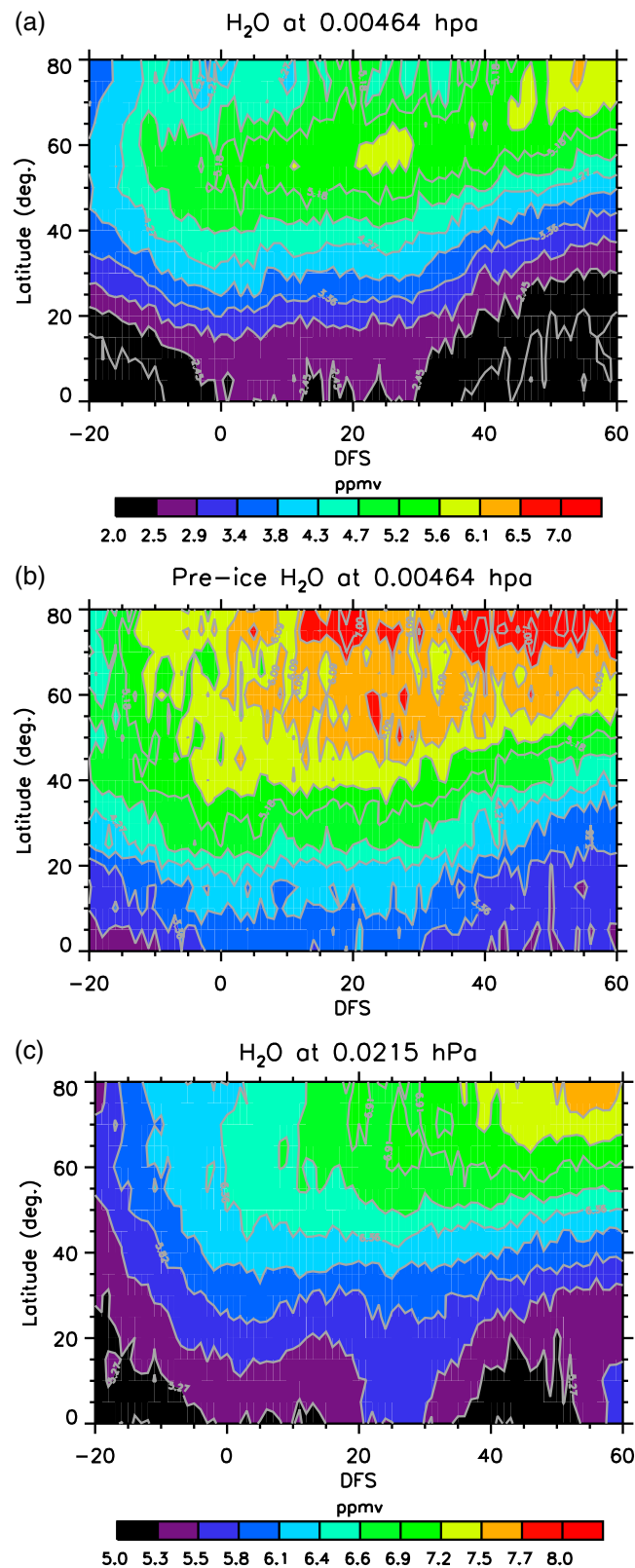
Figure 4. The latitude versus time cross sections of the zonal mean MLS H_2O in the summer of 2010. (a) For a given day on 0.00464 hPa surface, (20° longitude × 5° latitude) grid-mean values are used to calculate the zonal mean value. (b) Same as Figure 4a except that the grid-based pre-ice H_2O are used to calculate the zonal mean value. (c) Same as Figure 4a except that pressure level 0.0215 hPa is used.
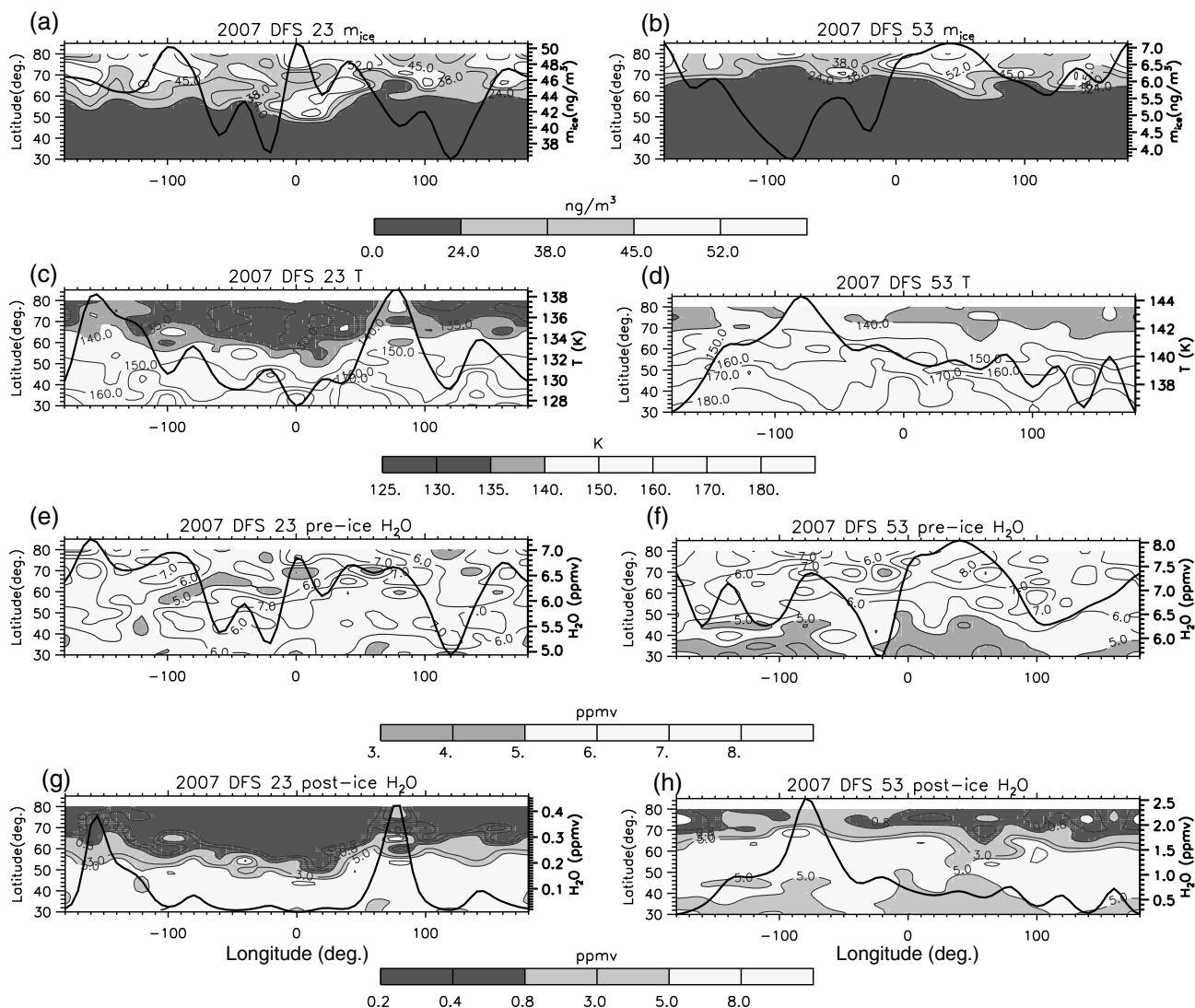
Figure 5. Similar to Figure 2 except for variables (a and b) m_{ice}, (c and d) temperature, (e and f) pre-ice H_2O, and (g and h) post-ice H_2O in the nominal 0-D case on 23 DFS (Figures 5a, 5c, 5e, and 5g) and 53 DFS (Figures 5b, 5d, 5f, and 5h).

season. Although at both the season start and end, the temperature should be warmer and approaching the frost point, the depletion zone is easier to form at the start because the total water vapor available is much lower at the start than at the end of the season. The pre-ice H_2O shown here is likely a more appropriate H_2O distribution of a cloud-free condition because it does not exhibit any polar depletion and it resembles the water vapor distribution right below the PMC layer, such as at 0.0215 hPa level (~77 km altitude), shown in Figure 4c.

5. Nominal 0-D Results and the 0-D Diagram

5.1. Nominal 0-D Results

The motive of using the 0-D model in this research is to reproduce the results shown in Figure 3 and to interpret how temperature and water vapor controls PMC daily global variation throughout the cloud season. The first set of 0-D model results is based on the original 0-D assumption; that is, 100% of the "excess H_2O" is turned into ice, referred to as nominal case hereinafter. The calculations are carried out on a daily basis for five northern seasons from 2007 to 2011. For individual days the zonal series averaged north of 70°N are formed and then correlation coefficients between different variables are calculated.
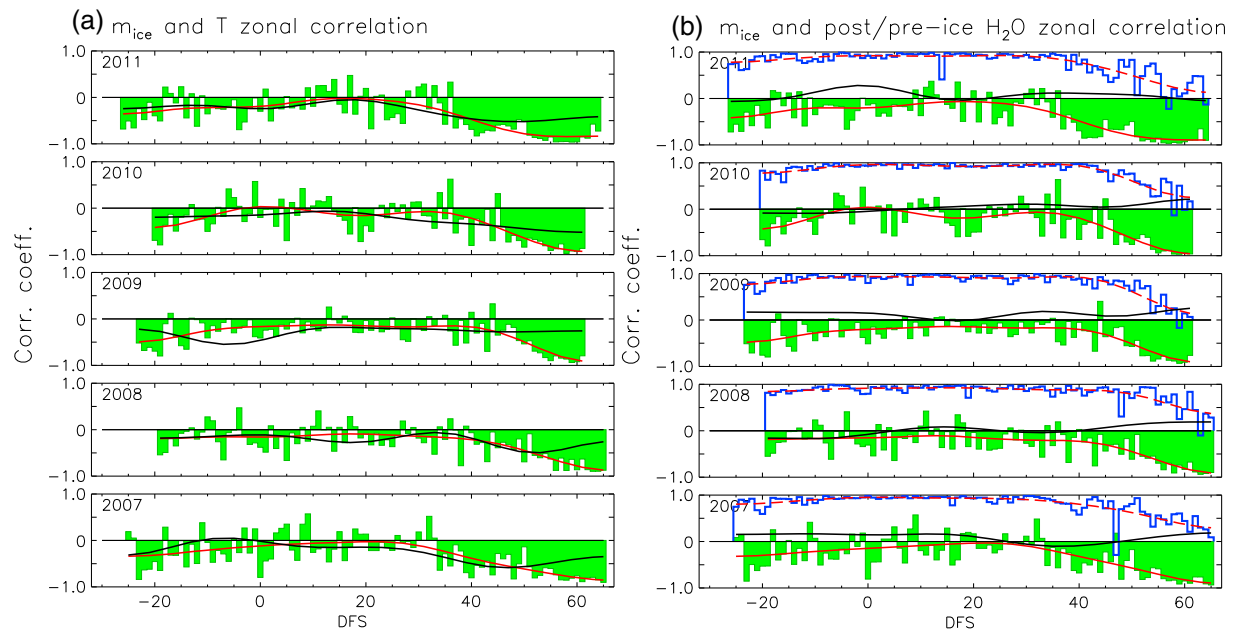
Figure 6. Intraseasonal variations of the correlation coefficients for the nominal 0-D model results. (a) The m_{ice} and temperature correlation. The green fill and red curves are daily and 16 day smoothed series, respectively. The black curve is the 16 day smoothed albedo and temperature correlation shown in Figure 3. (b) m_{ice} and pre-ice H_2O (blue and red dashed curves) and m_{ice} and post-ice correlation (green fill and solid red curves).

Model results for individual days are shown before the seasonal development of the correlation coefficients are examined. To compare with the observations shown in Figure 2, we chose model results for 23 and 53 DFS 2007. Figure 5 shows longitude versus latitude maps of m_{ice}, temperature, pre-ice, and post-ice H_2O. The post-ice H_2O global variation highly resembles the temperature field, as equation (2) shows that the post-ice H_2O equals to P_{SAT} in the nominal case. On both days there is a distinct depletion zone in the polar region. We have mentioned above that 0-D model overestimates the ice mass; therefore, the strong depletion feature is expected. Figures 5a–5d indicate that on large scales, brighter clouds and colder regions approximately coincide on both days, but on 53 DFS the correspondence is slightly better. The high correlation between m_{ice} and pre-ice H_2O on both days, indicated by the zonal series shown in Figures 5a, 5b, 5e, and 5f, suggests that pre-ice H_2O plays a strong role in controlling the m_{ice} variation. There are apparent resemblances between the 0-D modeled m_{ice} and the CIPS albedo (Figure 2). For example, on 23 DFS north of 70°N, both the 0-D result and the observation indicate that there is a m_{ice}/albedo increase in the longitude ranges around 150°W–100°W and 10°W–50°E, and in between it is a region of relatively low cloud brightness. However, the m_{ice} feature is noisier than in the observations because a selective pre-ice H_2O input is used in each grid box (see section 4). In addition, east of 120°E, the model result indicates another significant increase in the m_{ice}, while in the observation the increase of albedo is much weaker. This is caused by a difference in the temperature fields; Figures 5c and 2c show overall similar global variations, but the zonal series indicate that the model input temperature has a significant decrease at around 180°W/E that corresponds to the m_{ice} increase. Such a decrease is not obvious in the grid-mean temperature field. This temperature difference is not surprising because within each grid box, the maximum m_{ice} value usually corresponds to one of the colder events in that grid box.

Figure 6 shows the intraseasonal variation of correlation coefficients of m_{ice} versus temperature, 0-D post-ice H_2O, and 0-D pre-ice H_2O zonal series. Looking at the 16 day smoothed curves, we find that the m_{ice} and temperature correlation shown in Figure 6a agrees with the observations in Figure 3a, showing an overall anticorrelated relationship that is stronger at the start and end but poorer in the core of the season. The asymmetric start and end is also well reproduced. However, compared to the observations, the model results in Figure 6a show relatively clear separation between different stages of the season, with the correlation in the core of the season being distinctly poor. In addition, at the end of the season the modeled anticorrelation is stronger than in the observation and it monotonically approaches −1.0; while in the observation, the correlation coefficient starts to level off after 50 DFS. Similar to what is shown in the observations, an
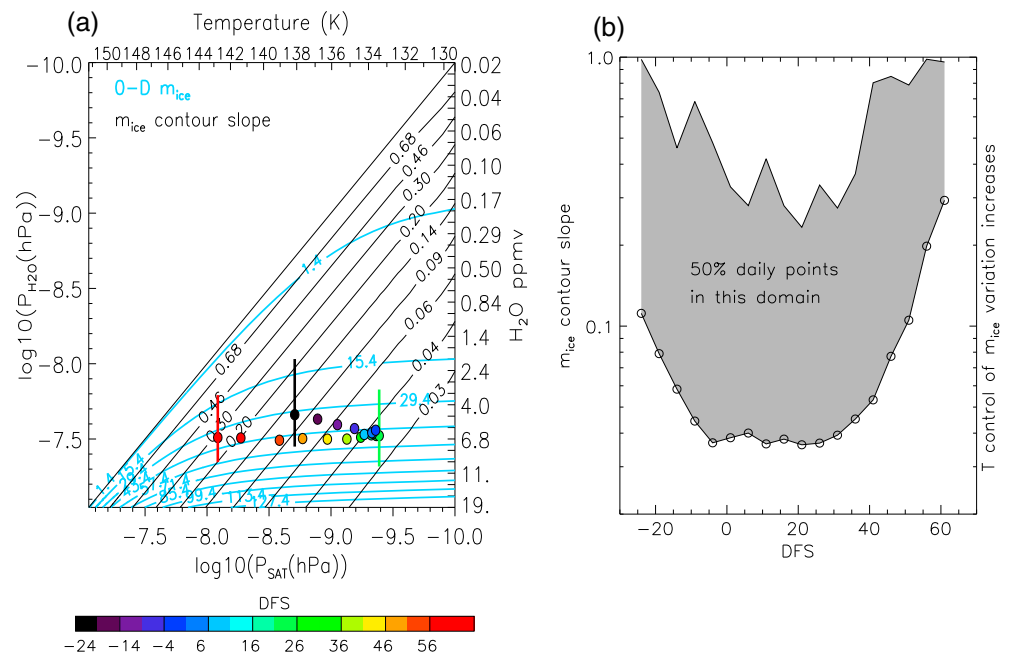
Figure 7. (a) The 0-D diagram on the $\log(P_{H2O})$ versus $\log(P_{SAT})$ space. When the m_{ice} contours (light blue) are increasingly parallel to the $\log(P_{SAT})$ axis, temperature change will have negligible impact on the m_{ice} variation. To describe this, m_{ice} contour slopes are given as the black lines. The diagonal line represents the contour slope of 1.0. Large colored dots are median point of nominal 0-D calculations for different day (with color) of the season. (b) Median and maximum contour slopes throughout the season. The large scatter (grey shade) suggests that role of temperature varies largely on the daily basis.

occasional stronger anticorrelation between m_{ice} and temperature can also occur in the core of season, such as during the 20 day period centered at 17–18 DFS in 2010. Such cases occur when cold and wet regions coincide. In the core of the season cold regions usually coincide with dry regions, because of dehydration; but on occasion many factors that are unaccounted for in the 0-D model can randomly combine to cause cold regions to coincide with wet regions. A more detailed analysis of the correlation between temperature and water vapor will be given in section 6.2.

The m_{ice} and post-ice H_2O correlation is highly similar to the m_{ice} and temperature correlation (see equation (2)), and the slight difference is caused by the fact that temperature and P_{SAT} zonal variations are not identical even if P_{SAT} is the sole function of temperature. Such a modeled m_{ice} and post-ice H_2O correlation apparently does not agree with the observation. In the core of the season the correlation coefficients in the observation and the model result are on the positive and negative sides respectively, but both suggest a poor correlation, while at the season start and end, the difference is especially large. As is mentioned above, the poor correlation between water vapor and albedo or m_{ice} seems to contradict the previous finding about water vapor playing a key role in determining the ice mass density. This discrepancy can be resolved by distinguishing between the pre-ice and post-ice H_2O. The key role of water vapor is reflected in the correlation of m_{ice} and pre-ice H_2O (blue curves in Figure 6b). The correlation remains close to 1.0 prior to 40 DFS and then gradually decreases toward the end of the season. This suggests that the results of the analysis depend on whether it is the pre-ice or post-ice H_2O that is being examined. Pre-ice and post-ice H_2O were not particularly distinguished in the previous studies because the depletion does not notably change the characteristics of the water vapor variation on longer time scales.

5.2. Relative Roles of Temperature and H_2O in the 0-D Diagram

The correlations shown in Figure 6 can be interpreted by the 0-D physics that addresses the relative roles of temperature and water vapor in different conditions. In Figure 7a we show the 0-D diagram that is similar to what *Rong et al.* [2012] has shown but with the nominal 0-D model results overlapped. From equation (1) we can see that P_{SAT} and P_{H2O} are in a linear combination to determine m_{ice} and therefore the same operator should be applied to both variables to examine their respective roles. We used logarithm because P_{SAT} varies

exponentially with temperature, and in practice, we choose to make temperature change linearly. 0-D modeled clouds only exist in the lower half of the plane, separated by the diagonal line at which P_{SAT} equals P_{H2O}. Looking at the m_{ice} contours we can clearly see that in the lower right corner, i.e., corresponding to brighter clouds or a colder and wetter environment, the m_{ice} contours are increasingly parallel to the P_{SAT} axis suggesting that temperature change will have only a negligible impact on the m_{ice} variation. On the contrary, when clouds get weaker, or the environment gets warmer and drier, the modeled m_{ice} will approach the $P_{SAT} = P_{H2O}$ line and temperature will have the largest possible control over the m_{ice} variation. The slope of the m_{ice} contour, defined as derivative $dlog_{10}(P_{SAT})/dlog_{10}(P_{H2O})$, is taken as a measure of the temperature control over m_{ice} variation, shown as thin black lines. The fact that such a slope is always smaller than 1.0 suggests that the importance of P_{H2O} always exceeds that of P_{SAT}, which explains why m_{ice} and pre-ice H_2O are highly correlated in Figure 6b. The large dots in Figure 7a correspond to daily median P_{SAT} and P_{H2O} for the given day, with the daily individual m_{ice} values being scattered around this point. The color of the dots represents the different stage of the season. The range of temperature axis, i.e., 130 K–150 K, is approximately the maximum temperature variation span for all modeled clouds, while the three vertical bars given at the start, core, and end of the season roughly cover the maximum range of H_2O variation, which is from ~1.4 ppmv to ~8.0 ppmv. We clearly see that these dots formed a "folded" line, i.e., at the start of the season it moves toward increasingly flattened m_{ice} contour slope, while after midseason it reverses its course to approach the $P_{H2O} = P_{SAT}$ line. At the start of the season, the condition is drier and colder than at the end, and the combined effect suggests a more flattened m_{ice} contour slope than in the end, which explains why the start and end are asymmetric. Figure 7b shows the intraseasonal variation of daily median and maximum values of m_{ice} contour slope. The gray shade in between marks a very large scatter, suggesting that the cloud population covers a wide range of brightness levels and environmental conditions on a given day. The seasonal development of the median slope reflects the changing importance of temperature in controlling the m_{ice} variation, while the large scatter explains why the transition between start, core, and end of the season is gradual.

5.3. Model Sensitivity to Temperature

Given the argument that the temperature control of m_{ice} variation increases when the environment is warmer and approaches the frost point, we conduct a sensitivity experiment via universally increasing the temperature by a 5 K and rerun the nominal case. Figure 8 shows the comparisons of the m_{ice} versus temperature correlations with and without +5 K, along with the 16 day smoothed curved in the observation (see Figure 3). It is clearly noted that the correlation of m_{ice} and temperature is systematically increased in the +5 K case regardless of the stage of the season. The regular model results without the temperature increase appear to show overall better agreement with the observation, especially at the season start. However, a key point worth noting in the +5 K case is that when temperature is warmer, the transition between the core and end is more gradual and furthermore at the season end, the correlation coefficient levels off after ~50 DFS, which is also shown in the observation. This suggests that a more rapid or earlier warming at the season end may lead to better agreement with the observation. The direct cause of the leveling off might be that when temperature is further increased to result in a larger fraction of the data points rising above the frost point, m_{ice} and temperature correlation will again decrease. This experiment also suggests that m_{ice} and temperature correlation can be used to diagnose how warm the environment is relative to the frost point. For example, revisiting Figure 3, we find that in 2009 the start of the season is more prolonged and is at least 10 days delayed compared to the rest of the years shown.

6. Zero-Dimensional Model Results Using an Adjusted Model Version

6.1. The m_{ice} and Water Vapor Correlation

The nominal 0-D model results did not successfully reproduce the albedo and H_2O correlation, with especially large discrepancies at the season start and end. To resolve this discrepancy and to improve the 0-D model performance, we include a factor to adjust the fraction of excess H_2O (F in equation (2)) that is turned into ice. The rationale for this approach lies in the fact that the 0-D model overestimates the ice mass in nearly all cases, which has been discussed on multiple occasions in related studies. *Hervig et al.* [2009] ran the 0-D model for July 2008 and concluded that at the m_{ice} peak ice equivalent H_2O VMR is overestimated by ~16%, which is roughly consistent with what *Rong et al.* [2012] found about the cloud peak m_{ice}. But the ~16%
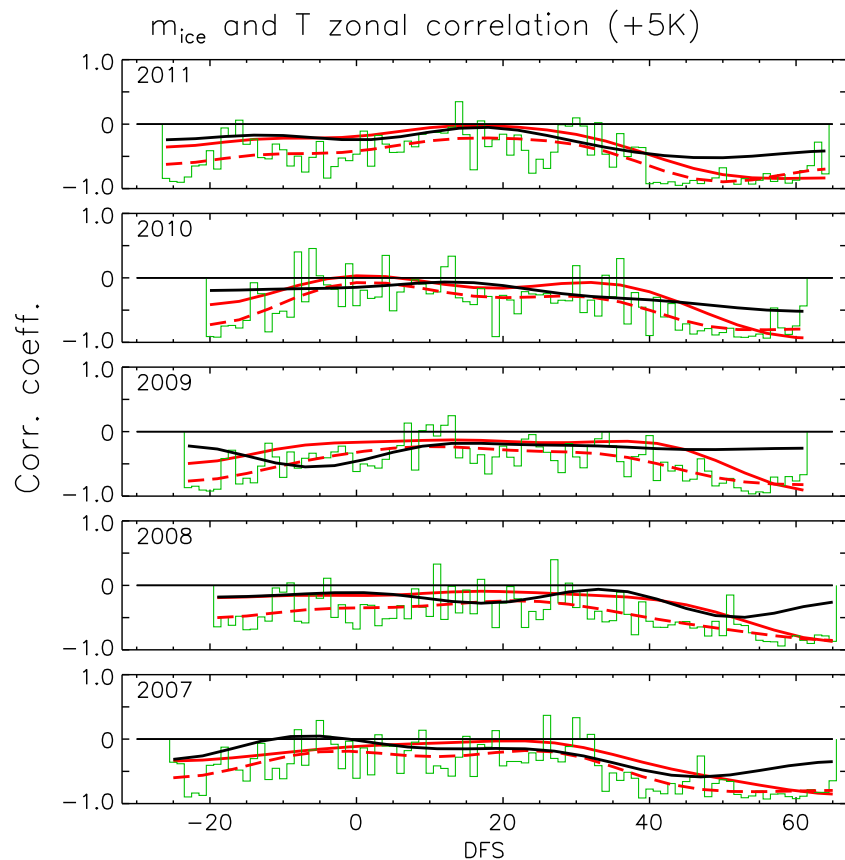
Figure 8. Sensitivity experiment with a systematically increased temperature. The thin green curves and dashed red curves are daily and 16 day smoothed m_{ice} and temperature correlation in the +5 K case. The solid red and black curves are 16 day smoothed m_{ice} and temperature correlation for the regular 0-D model and for the observation.

overestimate pertains only to strong clouds. If the clouds are systematically weaker, the extent of the overestimation should be reassessed. In general, the magnitude of the overestimate depends on a number of factors, such as the P_{SAT} formula selected, temperature or water vapor biases, and nucleation. For example, the *Murphy and Koop* [2005] version of P_{SAT} reduces the overestimate compared to the *Mauersberger and Krankowsky* [2003] version. Also, when temperature approaches the frost point, a small cold bias will significantly worsen the m_{ice} overestimate.

Among all these factors, neglecting the nucleation barrier will have the largest effect on the 0-D model results especially at the season start and end. In the framework of the classic droplet nucleation theory, when the temperature is closer to the frost point, the minimum supersaturation ratio required to grow an ice particle will be far greater than 1.0 because of the nucleation barrier [e.g., *Keesee*, 1989; *Rapp and Thomas*, 2006; *Hervig et al.*, 2009]. This suggests that the efficiency of ice production will be far lower than what the nominal 0-D assumption predicts at the season start and end. Therefore, adjusting the fraction of excess H_2O that is turned into ice is a reasonable measure to take, and meanwhile doing so will modulate the m_{ice} and post-ice H_2O correlation because this fraction adjusts the weighting between P_{SAT} and P_{H2O} in equation (2).

In this experiment the 0-D simulations were repeated, but with the restrictive condition that the m_{ice} and post-ice H_2O correlation coefficient must match the albedo and water vapor correlation coefficient on a daily basis within an absolute error of 0.01. The threshold of 0.01 for the correlation coefficient error was arbitrarily chosen except for the constraint that it be far smaller than 1.0. Each simulation was carried out by recursively adjusting F, until convergence was reached. But we make it clear at this point that the purpose of the exact match of the correlation coefficients on a daily basis is to reproduce the correlation of albedo and post-ice H_2O on a seasonal scale. The m_{ice} in the adjusted model version is simply the nominal m_{ice} times F.
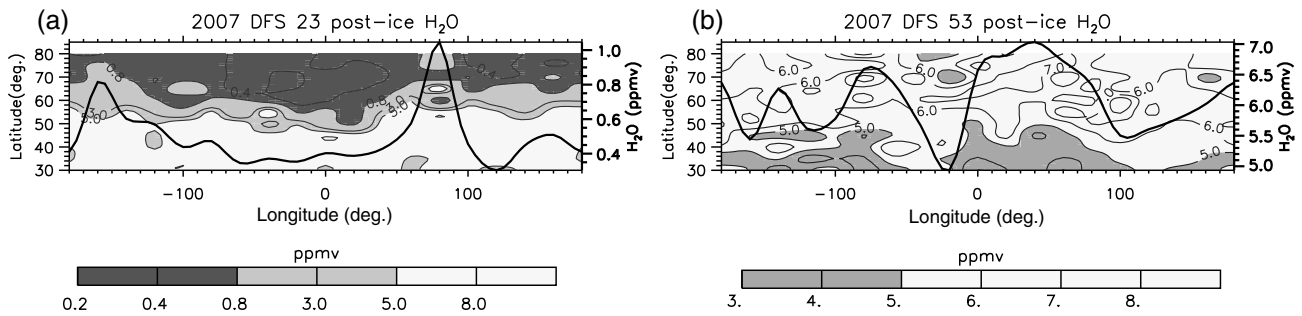
Figure 9. Similar to Figure 5 except for variables post-ice H_2O in the adjusted 0-D model version on (a) 23 DFS and (b) 53 DFS.

Therefore, the global variation of m_{ice} and the correlation between temperature and m_{ice} will remain unchanged from the nominal case.

Figure 9 shows the post-ice H_2O on 23 DFS and 53 DFS 2007, with F being 0.94 and 0.14, respectively. On 23 DFS it shows a strong polar depletion and it highly resembles the post-ice H_2O variation in Figure 5g. This is expected because on this day, F is close to 1.0 therefore it should be very close to the nominal case. On 53 DFS the post-ice H_2O is very similar to the preice H_2O shown in Figure 5f because only about 14% of excess H_2O is turned into ice. With such an adjustment, the post-ice H_2O shown here and the observed H_2O in Figure 2f also roughly agree, both indicating a wetter longitude section spanning 0°–100°E that corresponds to brighter clouds.

Figure 10 shows a correlation coefficient of m_{ice} and post-ice H_2O over the entire season. The albedo and H_2O correlation is overlapped to check on the convergence level on a daily basis. We can see that the
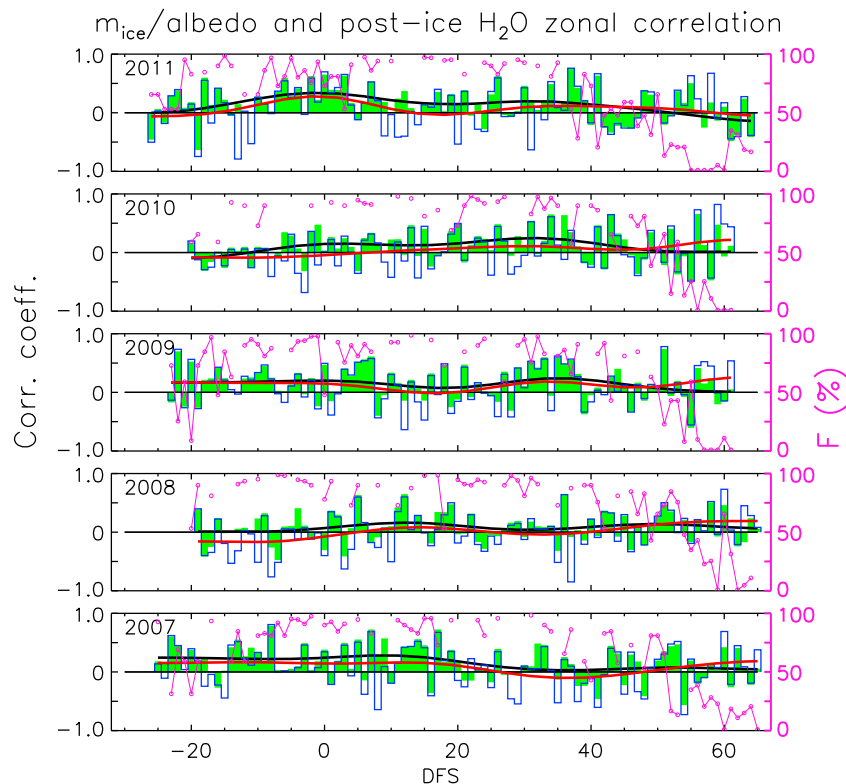

Figure 10. Intraseasonal variations of m_{ice} and post-ice H_2O correlation (green fill and red curve) for the adjusted model results. The daily excess H_2O fractions (F) are shown as pink symbols. The days with missing symbols are days with poor convergence levels. The albedo and H_2O correlation (blue and black curves) are overplotted to make comparisons.
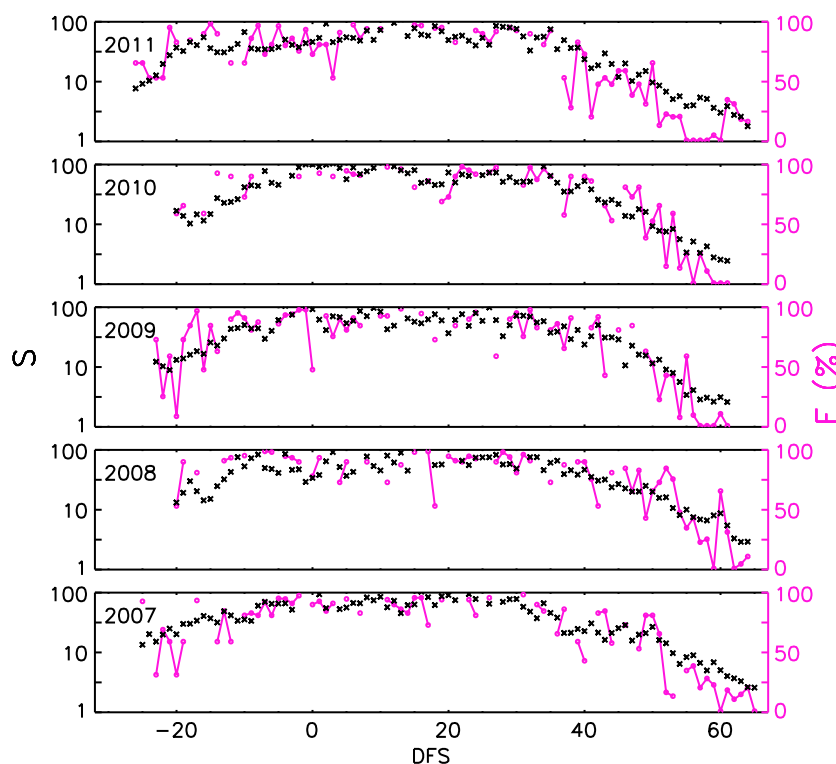
Figure 11. Intraseasonal variations of the "excess" H_2O fraction (F) used in the adjusted model version (pink) and the corresponding supersaturation ratios (S) averaged north of 70°N (black crosses). The S is calculated using the model input temperature and water vapor.

convergence level is generally satisfying but with some exceptions. The poor convergence occurs when the observed correlation coefficient cannot be reproduced because the required F to achieve the convergence is greater than 1.0. This can occur when the model input and the actual pre-ice conditions are significantly different. In reality, nevertheless, we are unable to verify this argument since the actual pre-ice temperature and H_2O that produced the observed cloud variation are impossible to retrieve. These poor convergence levels however do not affect the results in a qualitative sense since our goal is to reproduce the correlation between the cloud albedo and measured H_2O on a seasonal scale. But a notable effect of the poor convergence levels is that the model results lean toward positive correlations. Such a discrepancy suggests that there might be other factors beside the H_2O depletion that could have contributed to the poor correlation between the cloud brightness and water vapor.

The required daily F value remains as high as 90–95% from −15 to 40 DFS and decreases toward the start and end. The asymmetry between start and end is reflected, characterized by a more rapid decrease of F at the season start than at the end. The cause of this asymmetry should be consistent with the asymmetry of temperature and water vapor development throughout the season, as discussed above. Figure 11 shows the intraseasonal variation of supersaturation ratio (S) overlapped by F. For each day the same temperature and water vapor values that were fed into the 0-D model are used to calculate S, and then the daily averages are calculated. On a seasonal scale, the variation of S and F show a strong agreement, confirming what we argued above that a fraction far smaller than 1.0 is required at the season start and end when the supersaturation approaches 1.0.

6.2. Temperature and Water Vapor Correlation

At last we examine the correlation between temperature and water vapor before and after cloud production since we have argued above that the positioning of the maxima and minima of temperature and pre-ice H_2O in the zonal direction critically affects the m_{ice} zonal variation. In the summer mesosphere the meridional circulation driven by breaking gravity waves [*Garcia and Solomon*, 1985] generates a wet and cold environment in which the PMCs will form. But high H_2O and low temperature do not always coincide zonally
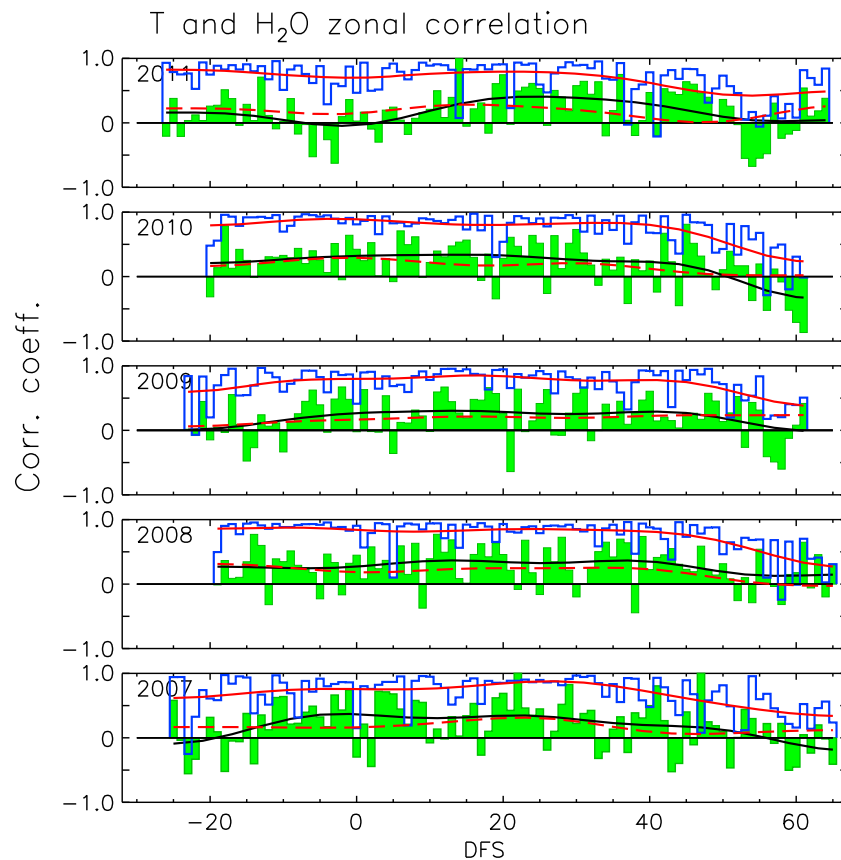
Figure 12. Intraseasonal variations of temperature and H_2O correlation. The green fill and the black curves: correlation coefficients of zonal series using the (20° longitude × 5° latitude) grid-mean values. In this case, H_2O profiles with the depletion features are included. Solid blue and red curves: post-ice H_2O and temperature correlation for the adjusted model results. Dashed red curves: the pre-ice H_2O and temperature correlation but shown only as the 16 day smoothed version.

because the H_2O depletion causes systematic shifting of the wet and cold sections. Furthermore, advection and wave activities will likely generate more zonal asymmetry and incoherence between temperature and water vapor. Figure 12 shows the correlation coefficients between MLS temperature and water vapor zonal variations using the grid-mean values north of 70°N, indicating a positive correlation except at the start and end of the season when the correlation is either reduced or negative. An overall positive correlation between temperature and water vapor exists because in the core of the season the colder regions are dehydrated by the ice production. The correlation of the model input temperature and post-ice H_2O in the adjusted model results is overlapped, indicating a very similar intraseasonal variation as in the observation but the correlation is much stronger. The stronger correlation exists in the model results because the 0-D model neglects the upwelling that persists throughout the season. The upwelling will lessen the depletion feature because it will recirculate the water vapor back to the cloud base. Other more comprehensive models such as CARMA will also generate stronger depletion feature if the simulation starts from the zero-ice condition on a daily basis and does not properly incorporate the longer time scale dynamical processes.

The dashed curves in Figure 12 are the 16 day smoothed correlation coefficients between the pre-ice H_2O and temperature. Since we have chosen measurements with the weakest depletion feature, the overall correlation appears poorer than the case with all measurements included (black), but the two curves remain very close to each other. As is shown in Figure 4b, in the latitudinal direction the chosen pre-ice H_2O does not show any depletion feature, indicating that wet and cold regions do coexist. Apparently in the zonal direction this is not the case. This suggests that ideal pre-ice H_2O conditions for the 0-D modeling is difficult to obtain because the actual cloud production does not operate like the 0-D model and there is no clear separation between pre-ice or post-ice states.

7. Conclusions

Daily zonal variations of CIPS cloud albedo and MLS temperature show a significant anticorrelation at the season start and end, but in the core of the season the anticorrelation is relatively poor. The albedo and water vapor show poor correlation throughout the season. A 0-D PMC model [*Hervig et al.*, 2009] was used to interpret these correlations and their intraseasonal variations. The relative importance of temperature and water vapor in determining the m_{ice} variation is assessed at different stages of the cloud season. 0-D simulations were carried out using MLS temperature and H_2O VMRs at a pressure level of 0.0046 hPa (~84 km) which is approximately the PMC centroid altitude. Ice mass density at this pressure level was used as the proxy for albedo since the main contribution to albedo comes from the ice mass at the cloud base where the largest ice particles exist. Zero-dimensional model physics indicates that when the environment is warmer and drier or the clouds are weaker, temperature takes an increasingly stronger role in determining the cloud brightness or m_{ice} variations, which explains the stronger anticorrelation at the season start and end. The strongest possible role temperature takes in controlling the m_{ice} variation is at the vicinity of $P_{H2O} = P_{SAT}$ line shown in the 0-D diagram. On the other hand, when the environment is colder and wetter or the clouds are stronger, the role of temperature becomes negligible in controlling the ice mass density variation. Water vapor takes on a strong role in all stages of the cloud season especially in the core of the season when the environment is colder and wetter. However, the dehydration or water vapor depletion causes systematic shifting of the zonal maxima of m_{ice} and post-ice H_2O, which explains the poor correlation of albedo and observed H_2O. Distinguishing the pre-ice and post-ice H_2O is critical to properly interpret the observed albedo and H_2O correlation in the zonal direction. Overall, the strong role of water vapor plays in controlling the m_{ice} variation is severely masked by the post-ice H_2O that is actually measured.

A +5 K increase is universally applied to all model input temperatures to further examine the role of temperature in determining the m_{ice} variation. The results show a systematic increase of the anticorrelation, which is expected based on 0-D model physics. But it is especially worth noting that such a warmer condition changes the transition between the core and end of the season, indicating a less distinct or more gradual transition. In addition, the +5 K case can reproduce the leveling off of the anticorrelation toward the season end shown in the observation. This suggests that earlier or more rapid warming may lead to better agreement with the observation.

To interpret the poor correlation of albedo and H_2O at the season start and end, we adjust the fraction of excess H_2O that is turned into ice (*F*) to match the modeled and observed correlations on a daily basis. Significantly reduced ice production efficiency, characterized by a smaller *F*, is required to achieve the convergence at the season start and end, which is supported by the nucleation theory suggesting that as the supersaturation ratio (*S*) approaches 1.0, the energy barrier will be higher for the ice particles to grow [e.g., *Keesee*, 1989; *Rapp and Thomas*, 2006]. The seasonal developments of *F* and *S* strongly agree, further validating the approach. The adjustment of *F* loosened the "locked" relationship between temperature and post-ice H_2O in the nominal 0-D case. A positive correlation exists between temperature and post-ice H_2O in the core of the season because the cold regions are depleted of water vapor, while at the season start and end such a relationship is poor because the ice production efficiency is reduced. The model results show a much stronger correlation than in the observation owing to the more intense water vapor depletion. The stronger water vapor depletion is probably caused by not properly including the seasonal-scale dynamical processes such as upwelling.

The fact that the 0-D model results can reproduce the correlation of daily global variations of PMCs with temperature and water vapor implies that microphysics is the main controlling mechanism in determining the cloud brightness or ice mass variations on planetary scales. The poor daily coincidences between AIM and Aura orbital tracks in the polar summer region did not change the qualitative agreement between the model results and the observations, which suggests that the global-scale cloud features are likely longer lived (i.e., up to one day) than the more localized small-scale cloud structures. The longer life time of the large-scale features is supported by the previous works indicating that both PMCs and temperature have shown planetary-scale varying modes such as 2 day and 5 day waves [*Merkel et al.*, 2008, 2009]. Although the more rapid dynamical processes such as advection and gravity waves may have contributed to the poorer correlations in the observations than in the model results, they do not change the conclusions in this study. Implementing the 0-D model has been successful in several PMC studies so far, but we should not overlook

the fact that it is highly simplified and has neglected the actual microphysical processes such as ice particle nucleation, growth, and sublimation. Interpretations of the 0-D model results based on the ice particle nucleation and growth are required. For example, the rationale of modulating the "excess" H_2O should be verified by the PMC models that include the ice particle nucleation and growth. Future studies include adopting a more comprehensive PMC model to verify what we found using the 0-D model and to assess the roles of other processes such as advection and gravity waves in affecting PMC global variations.

References

Bailey, S. M., C. A. Barth, M. J. Erickson, R. A. Kohnert, A. W. Merkel, E. M. Rodgers, S. C. Solomon, S. D. Straight, and J. E. Vian (1996), Science instrumentation for the Nitric Oxide Explorer, *Proc. SPIE Int. Soc. Opt. Engr.*, *2830*, 264–273.

Bailey, S. M. G. E., D. W. Thomas, A. W. Rusch, C. D. Merkel, J. N. Jeppesen, C. E. Carstens, W. E. Randall, J. M. McClintock, and J. M. Russell III (2009), Phase functions of polar mesospheric cloud ice as observed by the CIPS instrument on the AIM satellite, *J. Atmos. Sol. Terr. Phys.*, doi:10.1016/j.jastp.2008.09.039.

Baumgarten, G., A. Chandran, J. Fiedler, P. Hoffmann, N. Kaifler, J. Lumpe, A. Merkel, C. E. Randall, D. Rusch, and G. Thomas (2012), On the horizontal and temporal structure of noctilucent clouds as observed by satellite and lidar at ALOMAR (69N), *Geophys. Res. Lett.*, *39*, L01803, doi:10.1029/2011GL049935.

Benze, S., C. E. Randall, M. T. DeLand, G. E. Thomas, D. W. Rusch, S. M. Bailey, J. M. Russell III, W. McClintock, A. W. Merkel, and C. D. Jeppesen (2009), Comparison of polar mesospheric cloud measurements from the Cloud Imaging and Particle Size experiment and the solar backscatter ultraviolet instrument in 2007, *J. Atmos. Sol. Terr. Phys.*, *71*, 365–372, doi:10.1016/j.jastp.2008.07.014.

Benze, S., C. E. Randall, M. T. DeLand, G. E. Thomas, S. M. Bailey, J. M. Russell III, and A. W. Merkel (2011), Evaluation of AIM CIPS measurements of Polar Mesospheric Clouds by comparison with SBUV data, *J. Atmos. Sol. Terr. Phys.*, *73*, 2065–2072, doi:10.1016/j.jastp.2011.02.003.

Chandran, A., D. W. Rusch, G. E. Thomas, S. E. Palo, G. Baumgarten, E. J. Jensen, and A. W. Merkel (2012), Atmospheric gravity wave effects on polar mesospheric clouds: A comparison of numerical simulations from CARMA 2D with AIM observations, *J. Geophys. Res.*, *117*, D20104, doi:10.1029/2012JD017794.

Chu, X., C. S. Gardner, and G. Papen (2001), Lidar observations of polar mesospheric clouds at South Pole: Diurnal variations, *Gophys. Res. Lett.*, *28*(7), 1203–1206, doi:10.1029/2000GL012525.

DeLand, M. T., E. P. Shettle, G. E. Thomas, and J. J. Olivero (2003), Solar backscattered ultraviolet (SBUV) observations of polar mesospheric clouds (PMCs) over two solar cycles, *J. Geophys. Res.*, *108*(D8), 8445, doi:10.1029/2002JD002398.

Garcia, R. R., and S. Solomon (1985), The effect of breaking gravity waves on the dynamics and chemical composition of the mesosphere and lower thermosphere, *J. Geophys. Res.*, *90*(D2), 3850–3868, doi:10.1029/JD090iD02p03850.

Hervig, M. E., M. H. Stevens, L. L. Gordley, L. E. Deaver, J. M. Russell, and S. Bailey (2009), Relationships between PMCs, temperature and water vapor from SOFIE observations, *J. Geophys. Res.*, *114*, D20203, doi:10.1029/2009JD012302.

Hultgren, K., J. Gumbel, D. A. Degenstein, A. E. Bourassa, and N. D. Lloyd (2012), Application of tomographic algorithms to Polar Mesospheric Cloud observations by Odin/OSIRIS, *Atmos. Meas. Tech. Discuss.*, *5*, 3693–3716, doi:10.5194/amtd-5-3693-2012.

Jensen, E., and G. E. Thomas (1988), A growth-sedimentation model of polar mesospheric clouds: Comparison with SME measurements, *J. Geophys. Res.*, *93*(D3), 2461–2473, doi:10.1029/JD093iD03p02461.

Keesee, R. G. (1989), Nucleation and particle formation in the upper atmosphere, *J. Geophys. Res.*, *94*(D12), 14,683–14,692.

Lambert, A., et al. (2007), Validation of the Aura Microwave Limb Sounder middle atmosphere water vapor and nitrous oxide measurements, *J. Geophys. Res.*, *112*, D24S36, doi:10.1029/2007JD008724.

Llewellyn, E. J., et al. (2004), The OSIRIS instrument on the Odin spacecraft, *Can. J. Phys.*, *82*, 411–422.

Lumpe, J. D., et al. (2013), Retrieval of polar mesospheric cloud properties from CIPS: Algorithm description, error analysis and cloud detection sensitivity, *J. Atmos. Sol. Terr. Phys.*, *104*, 167–196, doi:10.1016/j.jastp.2013.06.007.

Mauersberger, K., and D. Krankowsky (2003), Vapor pressure above ice at temperatures below 170 K, *Geophys. Res. Letts. 30*(3), 1121, doi:10.1029/2002GL016183.

McClintock, W., D. W. Rusch, G. E. Thomas, A. W. Merkel, M. R. Lankton, V. A. Drake, S. M. Bailey, and J. M. Russell III (2009), The cloud imaging and particle size experiment on the Aeronomy of Ice in the mesosphere mission: Instrument concept, design, calibration, and on-orbit performance, *J. Atmos. Sol. Terr. Phys.*, doi:10.1016/j.jastp.2008.10.011.

Megner, L. (2009), Minimal impact of condensation nuclei characteristics on observable Mesospheric ice properties, *J. Atmos. Sol. Terr. Phys.*, *73*(14-15), 2184–2191.

Merkel, A. W., R. R. Garcia, S. M. Bailey, and J. M. Russell III (2008), Observational studies of planetary waves in PMCs and mesospheric temperature measured by SNOE and SABER, *J. Geophys. Res.*, *113*, D14202, doi:10.1029/2007JD009396.

Merkel, W. A., D. W. Rusch, S. E. Palo, J. M. Russell III, and S. M. Bailey (2009), Mesospheric planetary wave activity inferred from AIM-CIPS and TIMED-SABER for the northern summer 2007 PMC season, *J. Atmos. Sol. Terr. Phys.*, doi:10.1016/j.jasp.2006.05.01.

Murphy, D. M., and T. Koop (2005), Review of the vapour pressure of ice and supercooled water for atmospheric applications, *Q. J. R. Meteorol. Soc.*, *131*, 1539–1565.

Nielsen, K., D. E. Siskind, S. D. Eckermann, K. W. Hoppel, L. Coy, J. P. McCormack, S. Benze, C. E. Randall, and M. E. Hervig (2010), Seasonal variation of the quasi 5-day planetary wave: Causes and consequences for polar mesospheric cloud variability in 2007, *J. Geophys. Res.*, *115*, D18111, doi:10.1029/2009JD012676.

Rapp, M., and G. E. Thomas (2006), Modeling the microphysics of mesospheric ice particles: Assessment of current capabilities and basic sensitivities, *J. Atmos. Sol. Terr. Phys.*, *68*, 715–744.

Rapp, M., F.-J. Lübken, A. Müllemann, G. E. Thomas, and E. J. Jensen (2002), Small scale temperature variations in the vicinity of NLC: Experimental and model results, *J. Geophys. Res.*, *107*(D19), 4392, doi:10.1029/2001JD001241.

Rong, P., J. M. Russell III, L. Gordley, M. Hervig, L. Deaver, D. Siskind, P. Bernath, and K. A. Walker (2010), Validation of v1.022 mesospheric water vapor observed by the SOFIE instrument onboard the AIM satellite, *J. Geophys. Res.*, *115*, D24314, doi:10.1029/2010JD014269.

Rong, P., J. M. Russell III, S. M. Bailey, and M. E. Hervig (2012), The roles of temperature and water vapor at different stages of the PMC season, *J. Geophys. Res.*, *117*, D04208, doi:10.1029/2011JD016464.

Rusch, D. W., G. E. Thomas, W. McClintock, A. W. Merkel, S. M. Bailey, J. M. Russell III, C. E. Randall, C. Jeppesen, and M. Callan (2009), The cloud imaging and particle size experiment on the aeronomy of ice in the mesosphere mission: Cloud morphology for the northern 2007 season, *J. Atmos. Sol. Terr. Phys.*, doi:10.1016/j.jastp.2008.11.005.

Russell, J. M., III, M. G. Mlynczak, L. L. Gordley, J. J. Tansock, and R. W. Esplin (1999), Overview of the SABER experiment and preliminary calibration results, in *Proc. SPIE 3756*, Optical Spectroscopic Techniques and Instrumentation for Atmospheric and Space Research III, vol. 277, edited by A. M. Larar, Denver, Colo., doi:10.1117/12.366382.

Russell, J. M., III et al. (2009), Aeronomy of Ice in the Mesosphere (AIM): Overview and early science results, *J. Atmos. Sol. Terr. Phys.*, doi:10.1016/j.jastp.2008.08.011.

Schwartz, M. J., et al. (2008), Validation of the Aura Microwave Limb Sounder temperature and geopotential height measurements, *J. Geophys. Res.*, 113, D15S11, doi:10.1029/2007JD008783.

Solomon, S. C., et al. (1996), The Student Nitric Oxide Explorer, *Proc. SPIE Int. Sot. Opt. Eng.*, 2810, 121–132.

Summers, M. E., R. R. Conway, C. R. Englert, D. E. Siskind, M. H. Stevens, J. M. Russell III, L. L. Gordley, and M. J. McHugh (2001), Discovery of a water vapor layer in the Arctic summer mesosphere: Implications for polar mesospheric clouds, *Geophys. Res. Lett.*, 28(18), 3601–3604, doi:10.1029/2001GL013217.

Waters, J. W., et al. (2006), The Earth Observing System Microwave Limb Sounder (EOS MLS) on the Aura satellite, *IEEE Trans. Geosci. Remote Sens.*, 44, 1075–1092.